Three-dimensional tracking of microswimmer suspensions

Mehmood, Junaid; Muller, Koen; Kumar, Sowmya; Buchner, Abel John; Tam, Daniel

DOI
10.1007/s00348-025-04002-3

Publication date
2025

Document Version
Final published version

Published in
Experiments in Fluids

Citation (APA)
Mehmood, J., Muller, K., Kumar, S., Buchner, A. J., & Tam, D. (2025). Three-dimensional tracking of microswimmer suspensions. *Experiments in Fluids*, *66*(4), Article 81. https://doi.org/10.1007/s00348-025-04002-3

Experiments in Fluids (2025) 66:81
https://doi.org/10.1007/s00348-025-04002-3

RESEARCH ARTICLE

Three-dimensional tracking of microswimmer suspensions

Junaid Mehmood[1] · Koen Muller[1] · Sowmya Kumar[1] · Abel-John Buchner[1] · Daniel Tam[1]

Received: 21 November 2024 / Revised: 3 February 2025 / Accepted: 17 February 2025

Abstract

Understanding the locomotion of microorganisms is essential for insights into microbial ecology, infection, and colonization processes. Although two-dimensional microscopy has been widely used to study microswimmer motility, it does not capture the full extent of their three-dimensional (3D) movement. Recent advances in defocused particle tracking, holographic tracking velocimetry, and stereo-microscopy face challenges in achieving high resolution at larger particle densities and tracking multiple microswimmers in suspension. In this work, we introduce a novel multi-camera microscopy system that significantly improves the accuracy of 3D microswimmer tracking. Our system uses four sCMOS cameras to image microorganisms within a $2.5 \times 2.5 \times 2\ \mathrm{mm}^3$. We assess the performance of our microscopy system by tracking a population of the unicellular motile algae *Chlamydomonas reinhardtii*. An in-house tracking algorithm based on the projective geometry framework enables tracking with reprojection errors below 0.3 body lengths. This system supports imaging and tracking particle source densities of 0.32, higher than other existing single camera 3D microscopy techniques. Analysis of *C. reinhardtii* trajectories in 3D reveals a predominance of left-handed chirality and helical swimming patterns. Moreover, our 3D tracking data provide translational and rotational diffusion coefficients that differ from those obtained using traditional two-dimensional methods.

1 Introduction

The study of microbial ecology, colonization, and infection requires a fundamental understanding of the interactions between motile microorganisms and their physical environment, including surface interactions, accumulations, cell–cell interactions, and collective behavior. Tracking the motion and orientation of swimming microorganisms is, therefore, crucial to gain insights into their behavior and how they navigate through complex environments and respond to external stimuli such as light (Hill and Vincent 1993; Schaller et al 1997), gravity (Yoshimura et al 2003), chemical gradients (Alon et al 1999; Eisenbach 1999), and/or physical barriers (Harkes et al 1992; Bechinger et al 2016). Moreover, tracking microswimmers also has practical applications, including optimizing the design of bioreactors (Huesemann et al 2013; Pottier et al 2005), developing effective strategies for the treatment of infections (Shchelik et al 2021; Yan et al 2022), and monitoring the formation and dispersal of biofilms (Ralston and Swain 2009).

Microswimmers display a wide range of motility patterns, which are often three-dimensional (3D) in nature. For instance, bacteria navigate complex 3D environments through stochastic patterns of linear movements and sudden reorientations (Elgeti et al 2015; Constantino et al 2016). Protists, such as *Chlamydomonas reinhardtii*, display inherently three-dimensional helical swimming behavior (Rüffer and Nultsch 1985; Schaller et al 1997; Crenshaw et al 2000). Nevertheless, most studies focusing on microorganism locomotion have relied on two-dimensional optical microscopy as the primary tool for live imaging of microswimmers (Rothschild 1963; Feinleid and Curry 1971; Rüffer and Nultsch 1985; Leptos et al 2009; Kantsler et al 2013; Nakai et al 2015; Barry et al 2015; Jin et al 2020; Liu et al 2020; Coppola and Kantsler 2021), but two-dimensional microscopy does not capture the full range of the kinematics of microswimmers (Taute et al 2015).

To address these limitations, several techniques have been developed for 3D tracking of microorganisms. These include tracking microscopy (Berg 1971; Liu et al 2014), defocused particle tracking (DPT) (Speidel et al 2003; Wu et al 2005; Taute et al 2015), holographic tracking velocimetry (HTV) (Coëtmellec et al 2001; Cierpka and Kähler 2012), and stereomicroscopy (Baba et al 1991; Crenshaw 1996; Drescher et al 2009). These methods have provided

---

✉ Daniel Tam
d.s.w.tam@tudelft.nl

[1] Process & Energy, ME, TU Delft, Leeghwaterstraat 39, 2628 CB Delft, The Netherlands

valuable insights into the motility of various species. For example, tracking microscopy has been used to study bacteria such as *Escherichia coli* (Berg 1971, 2004; Mathijssen et al 2019) and *Caulobacter crescentus* (Liu et al 2014). DPT has been applied to examine the collective dynamics of E. coli (Wu et al 2006), to study variations in bacterial run-and-tumble behaviors (Taute et al 2015), and to measure the flow field around *Euglena gracilis* (Giuliani et al 2021). HTV has been used to study the motility of copepods *nauplius* (Sheng et al 2006), dinoflagellates (*Pfiesteria piscicida, Karlodinium veneficum, Prorocentrum minimum*) (Sheng et al 2007; Lee et al 2016), spermatozoa (Su et al 2012), and various bacterial species (*E. coli, Agrobacterium tumefaciens, Pseudomonas aeruginosa*) (Cheong et al 2015; Bianchi et al 2017). Stereo-microscopy has been used to study the three-dimensional trajectories of sea urchin larvae *Clypeaster japonicus* (Baba et al 1991) and green algae *Chlamydomonas reinhardtii* (Drescher et al 2009; Polin et al 2009).

These techniques have inherent limitations, however. Tracking microscopy is restricted to tracking one object at a time and can introduce background flow in larger chambers. DPT struggles with higher particle densities and is sensitive to low signal-to-noise ratios (Cierpka and Kähler 2012). HTV faces challenges with overlapping holograms and uncertainties along the optical axis (Gao et al 2013). Stereomicroscopy is limited to low particle densities to avoid false particle identifications and overlapping images (Elsinga et al 2006). For all these techniques, tracking multiple cells leads to high occlusion rates and results in low tracking certainty. Therefore, developing an experimental technique that can accurately track multiple microswimmers at higher densities is of great interest for studying important questions in biophysics, such as population behavior in complex three-dimensional environments encountered in nature and the characterization of cell-cell interactions.

Here, we present a unique four-camera microscopy system that builds on established macroscopic tracking methods, which often use 3-8 cameras for 3D tracking (Jahn et al 2021). In particular, the system introduces advances from 3D particle tracking velocimetry (3D-PTV) (Maas et al 1993; Malik et al 1993; Ouellette et al 2006; Attanasi et al 2015; Schanz et al 2016) and applies it to a single-objective multi-camera setup, previously used to perform tomographic particle image velocimetry (Tomo-PIV) in immersion droplets (Kim et al 2011). Our approach extends these techniques to the microscopic regime, enabling accurate 3D tracking of multiple microswimmers at low to medium densities. Specifically, we use four sCMOS cameras to image the same volume of $2.5 \times 2.5 \times 2$ mm^3. Our custom-developed tracking algorithm is based on the projective geometry framework, which supports fast and computationally efficient linear ray tracing. By tracking green algae *C. reinhardtii* at varying concentrations, we evaluate the performance and limitations of our tracking system and algorithm, and demonstrate a significant improvement over previous single-camera microscopy systems. We achieve accurate and reliable tracking at higher particle source density of 0.32, with a low reprojection error of 0.3 body lengths. Our experimental results reveal that *C. reinhardtii* cells exhibit predominantly left-handed chirality and swim in elongated helices with larger pitch and shorter radii, at a helical frequency of 1 to 2 Hz that is varying across the population. We also calculate the persistence length of microswimmer trajectories and cell diffusion coefficients, showcasing that 3D data are necessary to characterize the population behavior correctly.

2 Three-dimensional tracking setup

We track a suspension of microswimmers using a multi-camera microscope (Fig. 1), a three-dimensional tracking setup which is designed around a single common objective and includes a light source, four sCMOS cameras, and a flow chamber. The optical configuration is based on Kim et al (2011), Kim et al (2013) previously used for Tomo-PIV and 3D-PTV in immersion droplets and modified for an enlarged depth of field to consider suspension tracking in a approximately cubic domain.

The microswimmer suspension is illuminated with a laser, with a light diffuser (Optotune; LSR300) placed between the illumination source and the sample to reduce undesired speckles and provide uniform illumination by expanding the laser beam. The illumination intensity is modulated by the alignment of the diffuser on the optical rail. Our system supports both lasers and LEDs of different wavelengths. We use either green or red illumination, with wavelengths of 500 nm and 650 nm, respectively. The flow chamber containing the microswimmer suspension is fixed to a three-axis mechanical translation stage inside the illumination volume with 10 μm precision in the transverse direction.

Four cameras image the sample through a single common objective (Zeiss; $M = 1.5$, $f = 31$ mm), each camera collecting the light passing through a pinhole of diameter D_h. The cameras are all viewing the sample at an angle of 20° from the optical axis (Kim et al 2011). Because each camera's optical path is oriented off-axis, no transmitted light reaches the cameras directly and the cameras only collect forward scattered light by the cells. The imaging system is, therefore, similar to dark field microscopy, and cells appear as bright spots against a dark background as shown in Fig. 1c for each of the four cameras. The camera model used here is Imager sCMOS (2560×2160 pixels resolution with pixel size 6.5 μm^2, 16-bit dynamic range, maximum frame rate 50 fps).

The depth of field, Δz_o (Kim et al 2011), of the optical system can be adjusted between 6 mm and approximately

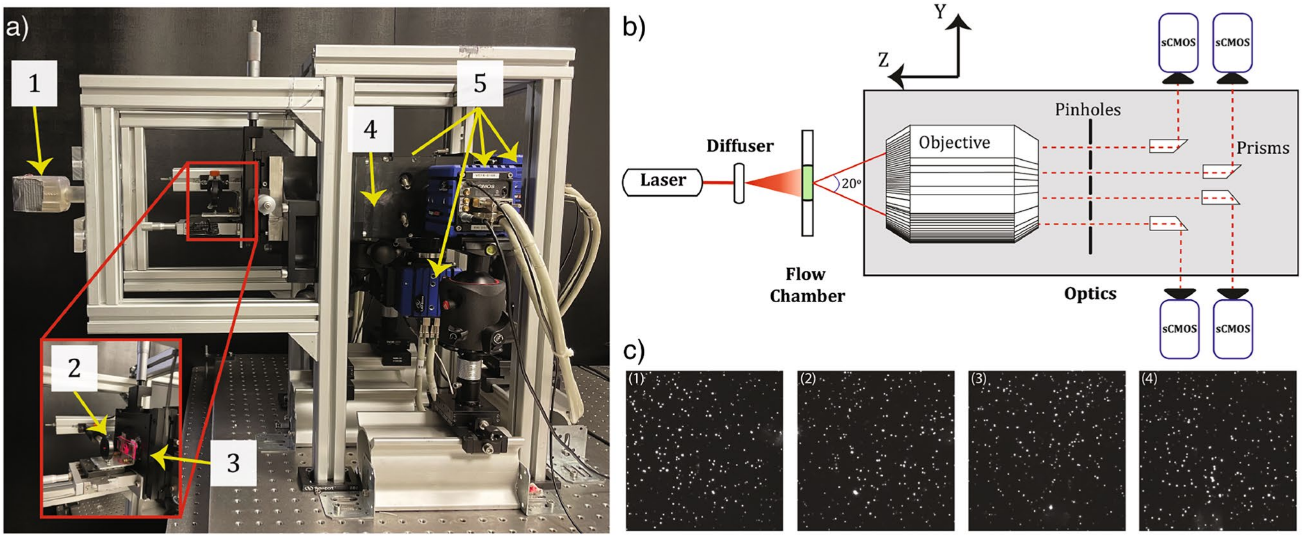

Fig. 1 Experimental setup. **a** The multi-camera microscopy setup: (1) laser, (2) light diffuser, (3) flow chamber and mechanical stage, (4) objective and optics, and (5) cameras. **b** Schematic of the multi-camera setup. Dashed red lines show the optical path. The laser light passes through the diffuser and illuminates the microswimmers inside the flow chamber. An objective of magnification $M = 1.5$ and focal length $f = 31$ mm collects the scattered light. The scattered light then passes through small pinholes, leading to a large depth of field. Prisms are used to guide the optical rays to the four sCMOS cameras. **c** The four camera views record an algae suspension of 5×10^4 cells/ml concentration. Bright dots represent the scattered light from individual illuminated cells. The number on each image corresponds to a specific camera

200 μm, by varying D_h. Due to our objective's low magnification, the cell image diameter, D_I, in our recordings is diffraction-limited. Following (Kim et al 2013), the diffraction-limited cell image diameter, D_L, is determined by the aperture size and the illumination wavelength. A reduced pinhole diameter, D_h, results in an increased cell image diameter, D_I, for a given swimmer size. For our tracking of *C. reinhardtii*, we use $D_h = 2$ mm, yielding $D_I = 9$ pixels and $\Delta z_o = 2$ mm, such that the entire flow cell is in focus and cells can be tracked throughout the entire chamber's depth.

3 Calibration procedure

We calibrate our tracking system with a custom-made calibration procedure, which uses a proprietary software calibration module (DaVis 8.4; LaVision GmbH) as a starting point and rewrites the mapping function in the projective geometry framework that is commonly used in computer vision (Hartley and Zisserman 2003).

A calibration target containing a regularly spaced 100 μm dotted grid pattern is positioned at the same location as the measurement volume of the flow chamber. Cameras are first focused and aligned to this grid using a large pinhole diameter of $D_h = 7$ mm that decreases the depth of field to 200 μm. Post-alignment, the pinhole diameter is decreased to $D_h = 2$ mm to achieve our experimental $\Delta z_o = 2$ mm depth of field. We acquired 13 images of the calibration target from each camera, translating the target through the measurement volume in 200 μm increments. This results in a calibrated measurement volume of depth 2.4 mm in the optical axis. We used the DaVis 8.4 calibration module to acquire both the coordinates of the images of the dotted pattern in the camera image planes of each camera and the corresponding world coordinates in the measurement volume.

The mathematical structure of the calibration mapping function used in this study is similar to that described by Muller et al (2020); however, unlike their method, which determines the mapping function from images of a freely moving calibration target with unknown position and orientation, in this work, we impose the target's positional displacements. The camera mapping function has two components: a linear part, which models the geometry of the optical setup and supports linear ray tracing, and a nonlinear part, which corrects for optical distortions. We first correct for optical distortions by computing a distortion correction map m that dewarps the calibration images to produce the distortion-corrected image. This step yields a function $\hat{\mathbf{x}} = m(\mathbf{x})$, which maps the coordinates in the camera image plane $\mathbf{x} = \begin{bmatrix} x & y \end{bmatrix}^T$ to distortion-corrected images $\hat{\mathbf{x}} = \begin{bmatrix} \hat{x} & \hat{y} \end{bmatrix}^T$. We then determine a mapping function $\hat{\mathbf{x}} = F(\mathbf{X})$ to map the coordinates $\mathbf{X} = \begin{bmatrix} X & Y & Z \end{bmatrix}^T$ of a point in the three-dimensional object domain to the dewarped projected image $\hat{\mathbf{x}}$. This function F is a linear function formulated within the projective geometry framework.

In this framework, augmented vectors facilitate the representation of points in both the image plane and the object domain. Specifically, in the dewarped image plane, coordinates are augmented into the ray-tracing vector $\tilde{\mathbf{x}} = \left[k\hat{x}\ k\hat{y}\ k\right]^T$, where k is a scaling parameter representing a coordinate along the principal optical axis, see Fig. 2. An inverse mapping $p(\tilde{\mathbf{x}})$ inverts this transformation, resulting in $\hat{\mathbf{x}} = p(\tilde{\mathbf{x}}) = \left[\tilde{x}/k\ \tilde{y}/k\right]$. Similarly, world coordinates $\mathbf{X}$ are augmented to obtain a homogeneous vector $\tilde{\mathbf{x}} = \left[X\ Y\ Z\ 1\right]^T$, simplifying geometric transformations in the calibration procedure. Figure 2 illustrates the relationship between these coordinate systems, showing the camera, the world coordinate system, and the dewarped image plane.

For each camera, the mapping function F models both extrinsic camera properties, i.e. the position and orientation of the camera, and intrinsic properties, i.e. optical properties and sensor properties. The extrinsic properties are represented by a rotation and translation $\left[\mathcal{R}\ \mathcal{T}\right]$, which represent the transformation from the world coordinates system to the camera coordinates system. Here, $\mathcal{R}$ is a 3 × 3 rotation matrix, and $\mathcal{T}$ is a 3 × 1 translation vector. The intrinsic properties are represented by a 3 × 3 camera matrix $\mathcal{K}$ of the form:

$$\mathcal{K} = \begin{bmatrix} fr_x & s & p_x \\ 0 & fr_y & p_y \\ 0 & 0 & 1 \end{bmatrix}. \tag{1}$$

Here f is the focal length of the lens in mm, r_x and r_y are the pixel pitch of the sCMOS sensor (px/mm), s is the pixel skew, and p_x and p_y are the coordinates of a point at the intersection of the principal optical axis and the dewarped image plane. With these notations, the mapping F can be written in the following form

$$\hat{\mathbf{x}} = F(\mathbf{X}) = p\left(\mathcal{K}\left[\mathcal{R}\ \mathcal{T}\right]\tilde{\mathbf{x}}\right). \tag{2}$$

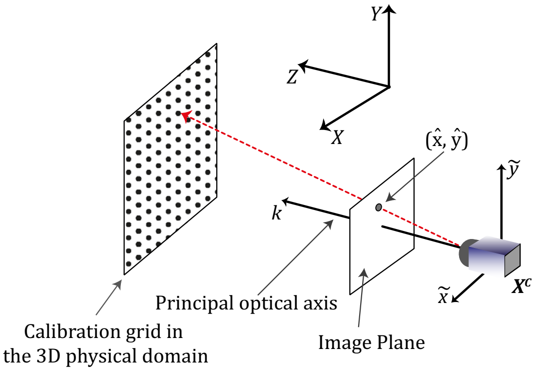

Fig. 2 Illustration of the optical path and calibration geometry. An optical ray, represented by the solid red line, extends from the camera center $\mathbf{X}^\mathbf{c}$ to a grid point location on the calibration grid in the three-dimensional object domain ($\mathbf{X} = \left[X\ Y\ Z\right]$). The camera's coordinate system is denoted as $\tilde{\mathbf{x}} = \left[\tilde{x}\ \tilde{y}\ k\right]$. The intersection of the optical ray with the dewarped image plane yields the coordinates $\hat{\mathbf{x}} = \left[\hat{x}\ \hat{y}\right]$

The calibration procedure determines, for each camera, the matrices $\mathcal{K}$, $\mathcal{R}$, and vector $\mathcal{T}$ and the parameters in the user prescribed distortion mapping. Representing the 3 × 4 projection matrix $\mathcal{P} = \mathcal{K}\left[\mathcal{R}\ \mathcal{T}\right]$, we use the DLT algorithm (Hartley and Zisserman 2003) between the augmented positions of the dots on the calibration target in the object domain $\tilde{\mathbf{X}}_j$ and the augmented coordinates of their images on the four cameras $\tilde{\mathbf{x}}_j^c$ to initiate its 12 elements. The four projection matrices $\mathcal{P}^c$ are then refined by solving a nonlinear least squares problem for each camera between the image coordinates and the projected positions from the object domain by:

$$\min_{\mathcal{P}^c} \sum_j \left\| \mathbf{x}_j^c - p\left(\mathcal{P}^c \tilde{\mathbf{X}}_j\right) \right\|^2. \tag{3}$$

Here superscript c is for cameras, and the subscript j denotes the calibration grid point number and includes all 13 positions of the target. Subsequently, a polynomial distortion mapping is applied that is solved between the projected object position and the image coordinates by a linear regression, and corrects for optical distortions in the microscope objective. Finally, an RQ decomposition is used to determine $\mathcal{K}$, $\mathcal{R}$, and $\mathcal{T}$ from the optimized projection matrices.

3.1 Accuracy of the camera calibration

We follow the approach described in Muller et al (2020) to assess the spatial accuracy of our calibration. Images of a dot from the calibration target on the camera's image planes are associated with four optical rays using projective geometry. For a perfect calibration, the optical rays from all cameras should intersect at a single point in the object domain. In practice, however, camera optical rays are skew lines and do not precisely intersect. We characterize the accuracy of the camera calibration by computing the skewness between these optical rays.

The skewness is evaluated by first triangulating the location of each calibration grid point in the object domain and then computing the average perpendicular distance of this point from the camera optical rays. For each of the 13 calibration target positions, we average the skewness corresponding to each dot on the target and present in Fig. 3 the average skewness as a function of the depth position Z. Our calibration procedure results in low triangulation errors, characterized by low skewness values: The minimum value was 0.3 μm at the center of the flow chamber, while the maximum value was 0.7 μm near the lower and upper surfaces

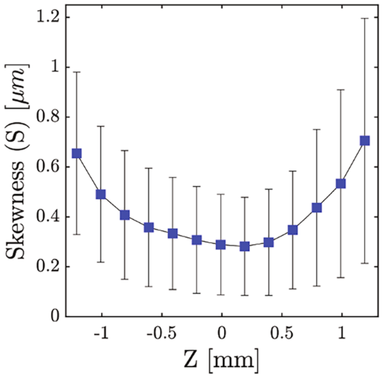

Fig. 3 Accuracy of camera calibration characterized by mean skewness for all grid points for four cameras along the Z-axis (optical axis). The error bars represent the standard deviation

of the viewing volume. These skewness values are an order of magnitude smaller than the diameter of the *C. reinhardtii* cell, indicating a high level of accuracy for our calibration.

4 *C. reinhardtii* tracking experiments

In this study, we tracked unicellular motile algae *Chlamydomonas reinhardtii* (wild-type CC125), obtained from the Chlamydomonas Resource Center. The cells were cultured following the protocols described by Quaranta et al (2015). Briefly, cells were grown phototrophically in Tris minimal medium with constant aeration via the injection of bubbles, at 24-26°C, with a 14/10-hour light/dark cycle at light intensity of 150 μmol·m^{-2}·s^{-1}. Cells were harvested during the exponential growth phase at a density of approximately 1×10^6 cells·ml^{-1}. Experimental concentrations ranging from 5×10^4 to 5×10^5 cells·ml^{-1} were achieved via dilution with Tris minimal medium.

Tracking experiments were performed in a custom-built flow chamber made from a 2-mm-thick transparent acrylic sheet (60 mm × 26 mm) with 8-mm laser-cut central chamber. The chamber was sealed with two glass coverslips using Norland optical adhesive (NOA81). To minimize flagellar adhesion (Mitchell 2000), the coverslips were cleaned and treated with a 1% bovine serum albumin (BSA)/phosphate buffer solution. Before each experiment, we transferred approximately 100 μl of algae solution using a micro-pipette and placed the flow chamber on the multi-camera microscope stage. We waited for 15 min before starting the recording to ensure that the cells acclimated to the environment in the flow chambers.

The algae suspension was illuminated with red laser light (PICOTRONIC; D1650) at wavelength $\lambda = 650$ nm, to prevent phototactic response (Harris 2009; Foster et al 1984). The camera sensors were cropped to 640 × 640 pixels to reduce the image size, resulting in a total viewing volume of $2.5 \times 2.5 \times 2$ mm^3. Images were acquired via a commercial PIV software (Davis 10; LaVision GmbH) at 20 fps with an exposure time of 42ms. The recording duration of each experiment was 5 min, corresponding to 6000 frames. Experiments were performed for cell suspension concentrations ranging from 5×10^4 to 5×10^5 cells/ml to characterize the performance of the setup. Figure 1c shows typical images of an algae suspension of 5×10^4 cells/ml from all four cameras.

The optical power output of the laser was 0.4 mW, and no active cooling was performed during the experiments. The background flow caused by the heating was characterized using passive tracer particles. A background flow with velocity magnitudes of 10-20 μm/s across the depth of field was observed. Using COMSOL Multiphysics® simulations, it was determined that this flow is driven by buoyancy forces arising from a temperature difference of approximately 1°C across the flow chamber. This background flow corresponds to a shear rate of 0.02 s^{-1}, which does not affect the population behavior of *C. reinhardtii* (Barry et al 2015).

5 Lagrangian particle tracking

We developed a custom particle-tracking algorithm that incorporates advances from bird tracking (Attanasi et al 2015), integrating progress in predictive tracking of passive tracers (Schanz et al 2016), and makes full use of the projective geometry framework (Hartley and Zisserman 2003) to achieve accurate three-dimensional trajectories of the cells. With projective geometry, we leverage the accuracy of our calibration and use linear ray tracing, leading to linear mathematical operations throughout the tracking process, which optimizes performance and reduces computational complexity. A detailed description of the algorithm can be found in Muller (2023); here, we provide an overview of the algorithm's important steps that are relevant to the subsequent part of this work. The Lagrangian particle tracking (LPT) algorithm is subdivided into five steps: particle identification, image tracking, coordinate matching and triangulation, time-resolved tracking and optimization, and post-processing.

5.1 Particle identification

The first step in our tracking algorithm is particle detection, which involves identifying the positions of cells in the camera image planes at each time step. We first dewarp the camera images by applying the distortion correction obtained from the calibration procedure (see section 3). We then represent the outer contour of the algae cell images in each camera view as conics (Hartley and Zisserman 2003) in terms of homogeneous coordinates as:

$$\tilde{\mathbf{x}}^T \mathbf{C} \tilde{\mathbf{x}} = \begin{bmatrix}\hat{x} & \hat{y} & 1\end{bmatrix} \begin{bmatrix} C_1 & C_2/2 & C_4/2 \\ C_2/2 & C_3 & C_5/2 \\ C_4/2 & C_5/2 & C_6 \end{bmatrix} \begin{bmatrix}\hat{x} \\ \hat{y} \\ 1\end{bmatrix} = 0. \tag{4}$$

Here, $\tilde{\mathbf{x}}$ is a vector of homogeneous coordinates, and $\mathbf{C}$ is a 3×3 symmetric matrix that defines the conic in the image plane.

The values of the coefficients C_i are determined by a second order Savitzky–Golay image smoothing and differentiation kernel (Meer and Weiss 1992) using a characteristic kernel size corresponding to the size of the cell image. We then calculate the midpoints of the conics to track the position of each algae cell as follows:

$$\begin{bmatrix}\hat{x}_o \\ \hat{y}_o\end{bmatrix}_j = - \begin{bmatrix} 2C_1 & C_2 \\ C_2 & 2C_3 \end{bmatrix}_j^{-1} \begin{bmatrix} C_4 \\ C_5 \end{bmatrix}_j . \tag{5}$$

Here, $\hat{x}_o^j$ and $\hat{y}_o^j$ represent the x and y coordinates of the midpoint of the j-th conic in the dewarped image plane.

Due to the three-dimensional motion and rotation of *C. reinhardtii*, the algae images exhibit strong fluctuations in size and intensity, appearing as blinking dots (Fig. 4a). This affects the peak detection algorithm. To address this, we use a multi-kernel approach using kernel sizes of 5×5, 7×7, and 9×9, deriving three outer contours for each image. The coefficients C_i are determined through a voting criterion that maximizes the average intensity within each kernel size.

Figure 4b shows a typical image, the detected cells, and their midpoints. The inset, Fig. 4c, corresponds to the same algae as those from Fig. 4a. Figure 4d demonstrates the robustness of our algorithm, where images of two overlapping algae are detected separately.

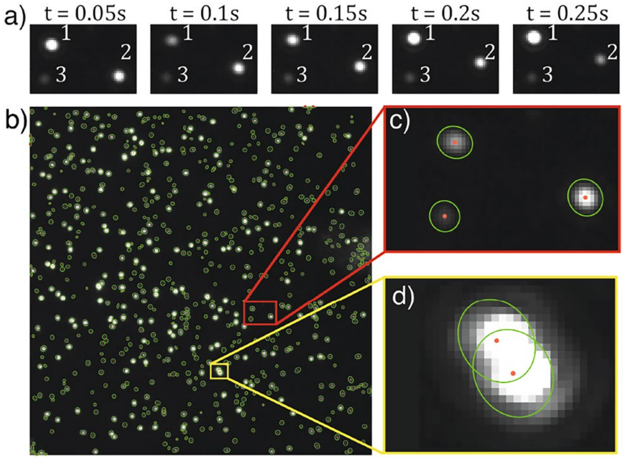

Fig. 4 **a** Images of three algae cells at different time steps showing variation in their image size due to the cell movement across the depth of field. Moreover, the cell blinking effect is visible for algae 1 and 2, where the intensity of the bright spot changes from one time step to the next due to cell rotation. **b** Camera image with detected algae cells represented by green conics. Red dots show the midpoints of the conics. **c** A close-up of detected algae cells for the same cell images from panel (a). **d** Identification of the cells for overlapping cell images

5.2 Image tracking

In the second step of our tracking algorithm, we track the movement of algae cells, here referred to as particles, in each camera view. Our approach involves identifying particle images in frame $n + 1$ within one body length of those in frame n. We do this by evaluating the distance between midpoints of particle images on the conics as

$$L_p = \sqrt{1 - \frac{\tilde{\mathbf{x}}_{o,n+1}^T \, \mathbf{C}_n \, \tilde{\mathbf{x}}_{o,n+1}}{\tilde{\mathbf{x}}_{o,n}^T \, \mathbf{C}_n \, \tilde{\mathbf{x}}_{o,n}}}. \tag{6}$$

Here, L_p is the distance between two particle images' midpoints, $\hat{\mathbf{x}}_{o,n}$ and $\hat{\mathbf{x}}_{o,n+1}$, in frame n and $n + 1$, respectively, normalized by the size of the particle image in frame n. If $L_p < 1$, the particle in frame $n + 1$ lies within the conic in frame n and is considered part of the track for that specific conic.

The threshold $L_p < 1$ is chosen based on our high temporal resolution, which results in minimal temporal displacement of particle images between frames. We measure a maximum displacement of approximately 1.5 pixels per frame. Normalizing this value by the average minimum distance between particles, calculated for a concentration of 5×10^4 cells/ml, yields 0.083. Even at the highest examined cell concentration, the maximum normalized displacement is 0.15. This parameter, known as the inverse of the particle spacing displacement ratio, quantifies the difficulty of particle tracking, with lower values indicating easier tracking (Malik et al 1993; Ouellette et al 2006). Since particle displacement remains small relative to inter-particle distance, $L_p < 1$ ensures robust tracking. However, this threshold can be adjusted for larger displacements, such as under superimposed flow.

The image tracking step results in an indexed list of two-dimensional tracks, including particle conic and midpoint information for each particle for all cameras. Occlusions may result in one detected particle becoming part of two tracks; in such cases, the track splits at the point of overlap, and a single particle is tracked by multiple track segments. Unique tracks are recovered for each particle during an optimization step discussed later. Figure 5 demonstrates the effectiveness of the image tracking algorithm in accurately capturing the motion of algae cells in a 50-frame

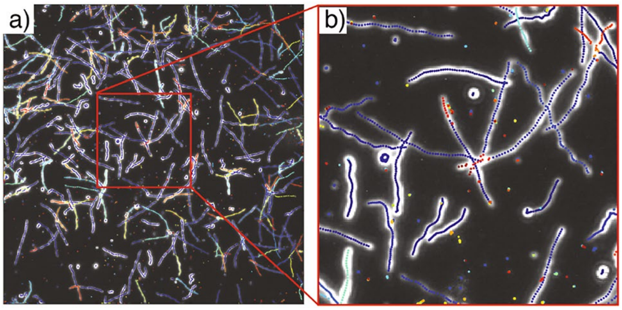

Fig. 5 Visualization of two-dimensional image tracking. **a** An average image created from 50 individual camera images, temporally spaced by $\Delta t = 0.05$ s, forming a time series, displaying particle motion as streaks with 2D tracks of each particle overlaid in distinct colors. **b** A zoomed-in view of the particle motion as streaks and their corresponding 2D tracks, including short tracks resulting from false particle identifications due to image noise

sequence for one of the cameras. The figure highlights that most trajectories correspond to real particles and effectively track their motion. A few short tracks are also reconstructed that do not correspond to actual particles because of image noise. These false particle identifications and trajectories are removed in the post-processing step.

5.3 Correspondence matching and triangulation

The next step in our tracking algorithm involves matching particle images across different cameras using epipolar geometry (Hartley and Zisserman 2003). Specifically, given a particle image in one camera, its corresponding image in a second camera must lie along the epipolar line, i.e. the projection of the optical ray from the particle through the center of the first camera onto the second camera's image plane. To establish correspondences, we compute the epipolar line in the second camera corresponding to each particle image in the first camera. We then calculate the distance between this epipolar line and all particle images in the second camera. Ideally, the correct particle image would lie exactly on the epipolar line, but due to noise and calibration errors, we allow a threshold distance of half body length. If the distance between a particle image and the epipolar line is less than this threshold, we consider it a match and establish a correspondence.

Establishing reliable correspondence between particle images in different camera views requires that each particle image lies within one body length of the epipolar line associated with the corresponding particle image in another camera. When this bi-directional condition is met, we consider the particle images to be matched, forming a stereoscopic correspondence. In a four-camera setup, multiple epipolar line combinations are possible. Trifocal correspondences between particle images in three views imply a stereoscopic correspondence for each two-view combination. Quadri-focal correspondences extend this to all four cameras. To limit false correspondences, arising from noise, occlusion, or calibration errors, we exclude stereoscopic correspondences and only process particles with trifocal or Quadri-focal correspondences.

After matching particle images across multiple cameras, we triangulate the particle's 3D position, $\mathbf{X}$, by minimizing the sum of squared distances between $\mathbf{X}$ and the optical rays from each camera, see (Muller et al 2020) for more details.

5.4 Time resolved tracking and optimization

Next, we combine the two-dimensional tracking and the particle image correspondences to obtain continuous trajectories in three dimensions.

In the first recorded frame, we initiate three-dimensional trajectories from each triangulated 3D particle location, from which trajectories are temporally extended using both the 3D object and the 2D image plane tracking information: At each frame, existing 3D object and 2D image plane trajectories are represented using a polynomial fit, with which we predict candidates for the particle image position in the subsequent frame. Based on these predictions, we find particle images within one body length in the next frame. This prediction step is particularly beneficial in instances of image occlusion, allowing us to find the particle image even when occlusion occurs.

As each frame is processed, new particle images are identified and appended to their corresponding trajectories. For each of these images, we triangulate their location in three-dimensions using image correspondences and subsequently calculate the re-projection error. Only the particle locations with an average re-projection error (evaluated across all cameras) that is less than one body length get incorporated into the three-dimensional trajectories. This iterative approach continues for all frames, appending trajectories accordingly.

These steps result in a set of feasible trajectories for each particle image. Any single particle might still be part of multiple candidate trajectories due to occlusions and imperfect correspondences arising from calibration errors. To solve this, we implement a cost-function solution that rewards longer trajectories, matched number of image correspondences (tri-focal and quadri-focal), and low re-projection error. Employing a divide-and-conquer strategy inspired by Attanasi et al (2015), we find a solution that best fits simultaneous tracking in the object and image domains. Once the optimization is complete, we obtain unique indices for each trajectory and their respective image plane and three-dimensional locations.

Figure 6a illustrates the result of our tracking algorithm after step 4, tracking cells over 50 frames at 5×10^4 cells/

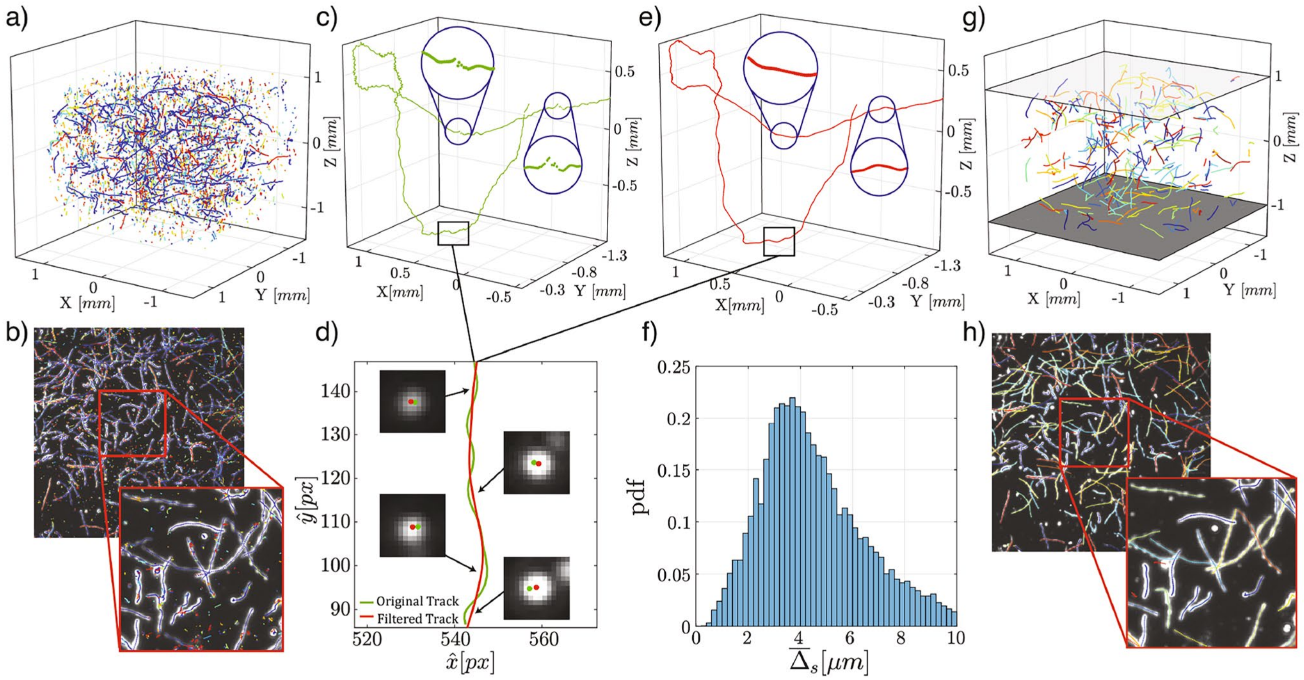

Fig. 6 **a** Triangulated positions in the object domain for 50 frames at a cell density of 5 ×10^4 cells/ml. Longer trajectories appear in the center, where the viewing volume is located (2 mm depth), while shorter ones are predominantly ghost trajectories. **b** An average intensity image of the same 50 frames, overlaid with 2D projections of algae trajectories. The inset shows a close-up of the region within the red rectangle. **c** A representative 3D cell trajectory with discontinuities (circular insets) caused by occlusions and imperfect matching; the rectangle indicates the portion of the trajectory re-projected in (d). **d** Two-dimensional re-projections of the trajectory in (c) and (f), before and after applying a third-order Savitzky–Golay filter (kernel length 25) to correct blinking artifacts. The insets display the re-projected positions of the original and filtered trajectories at selected time steps. **e** The fully filtered 3D trajectory. **f** Distribution of the time-averaged difference $\overline{\Delta}_s$ between original and filtered trajectory locations in object space for all trajectories. **g** Cleaned and filtered trajectories from the same 50-frame time series, with gray planes marking the top and bottom of the flow chamber. **h** The same average intensity image as in (b), now overlaid with re-projected 3D trajectories. Bright spots without overlaid tracks are dust particles or immobile cells; the inset zooms in on the same region highlighted in (b)

ml concentration. For 6000 frames, which corresponds to 5 min of recording, we obtain approximately 0.8 million trajectories with an average track length of 10 frames. Many of these trajectories are ghost tracks or associated with spurious identifications (see Fig. 6b). We filter out these trajectories in the post-processing step, as discussed below.

5.5 Post-processing

The robust and thorough nature of our tracking algorithm ensures that minimal data are lost during tracking. However, this results in a high number of unphysical trajectories, such as ghost particle trajectories (see Fig. 6b). To address this, we remove spurious trajectories in a post-processing step. First, we reduce the tracking dataset by filtering trajectories based on length: tracks shorter than 20 frames are discarded. This filtering step effectively removes most ghost trajectories, as ghost particles lose correspondences within ten frames resulting in shorter tracks. Next, we remove tracks corresponding to immobile cells, such as those stuck on solid surfaces, which are identified by way of their positional standard deviation; tracks with a standard deviation below 20 μm are removed. Finally, we discard tracks for particles moving faster than 250 μm/s, which is much greater than the typical algae swimming speed of 100 μm/s (Crenshaw et al 2000).

The remaining trajectories are filtered in order to reduce the noise resulting from calibration errors, occlusions, and inaccuracies in the triangulated position due to cell blinking in at least one camera view. Figure 6c displays a representative cell trajectory illustrating these artifacts. The position triangulated in step 3 is influenced by minor differences in midpoints across various cameras caused by the blinking effect, leading to a shift in the triangulated position from one frame to another and generating an apparent high-frequency helical motion. This can be seen when inspecting a portion of the track (indicated by a rectangle) projected onto the image plane (Fig. 6d). Camera images are also presented in the inset at different points along the track. The reconstructed cell trajectory is marked with green dots in Fig. 6d and can be seen to oscillate from one side of the particle image to the other. It is clear that this oscillation is not physical. The re-projected position oscillates from one side of the algae image to the other because of the cell blinking effect in another camera view. Another artifact is the discontinuity of the trajectory, highlighted by circles in Fig. 6c, which arises from occlusions and imperfect matching at these positions. To correct for this noise, we apply a 3rd order Savitzky-Golay filter with kernel length of 25. The filtered track is represented in Fig. 6e, and its re-projected location is displayed in Fig. 6d with a red line and red dots on the camera images. Figure 6d shows that the re-projection of the filtered trajectory aligns with the particle's image center, thereby validating our filtering approach. We characterize the difference between the filtered track and the original track by computing a time-averaged difference as $\overline{\Delta}_s = \frac{1}{N}\sum_{t=1}^{N}\left|\mathbf{X}_t - \mathbf{X}_t^s\right|$, where $\mathbf{X}_t^s$ represents the filtered track position. Figure 6f displays the distribution of average differences for all trajectories. The mean value for the $\overline{\Delta}_s$ distance is 4.5 ± 1.9 μm, which is on the order of the algae cell's radius. This indicates that the filtering does not affect the trajectory's helicity but mainly corrects errors due to the blinking effect.

Finally, we apply a linear correction to the position in the Z direction to rescale the depth of the flow chamber, accounting for the difference in the index of refraction between the calibration procedure and the experiment. The calibration was performed using a calibration target in ambient air, whereas the experiments were conducted in a flow chamber filled with an aqueous Tris solution. The higher index of refraction of the Tris solution causes a spatial compression along the optical axis, necessitating this correction. The correction was performed using experimental data as follows:

We first identify the locations of the upper ($\mathcal{Z}_u$) and lower ($\mathcal{Z}_l$) surfaces in the compressed frame of reference by identifying cells stuck to the surfaces of the top and bottom coverslips. These cells display minimal movement (V <20 μm/s) compared to motile cells in the bulk. We fit a plane through these immotile cells to determine the upper and lower surface locations. Once the surface locations are known in the compressed frame of reference, the correction is applied as

$$Z_{corrected} = \mathcal{Z}_L + \left(\frac{\mathcal{Z}_U - \mathcal{Z}_L}{\mathcal{Z}_u - \mathcal{Z}_l}\right)(Z - \mathcal{Z}_l)$$

where $\mathcal{Z}_U = 1$ and $\mathcal{Z}_L = -1$ define the true upper and lower surface locations.

It is worth noting that this linear correction assumes that all optical rays follow the same path. However, variations in path lengths through the glass and suspension may occur across different areas of the image, which would result in non-parallel detected surfaces. However, within the bounds of our experiments, we do not observe such deviations: the fitted planes corresponding to the upper and lower surfaces remain parallel. This suggests that any errors introduced by these effects are negligible, and the linear correction accurately accounts for the difference in refractive index.

Table 1 Average number of detected particles and the particle source density across all cameras and frames for different cell concentrations

No	Concentration (cells/ml)	Detected particles	N_S
I	5×10^4	705	0.109
II	1×10^5	1176	0.182
III	2×10^5	2082	0.323
IV	5×10^5	4340	0.674

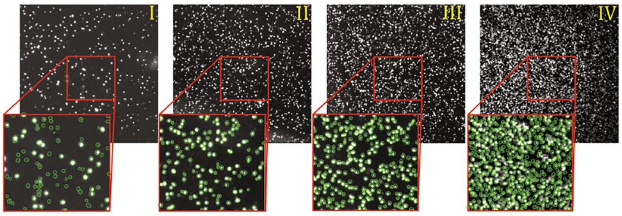

Fig. 7 Sample camera images for varying cell concentrations: I. 5×10^4 cells/ml, II. 1×10^5 cells/ml, III. 2×10^5 cells/ml, IV. 5×10^5 cells/ml. Close-ups show the detected cells in part of each image

Figure 6g shows the filtered three-dimensional trajectories in the corrected frame of reference for cell density of 5×10^4 cells/ml. For clarity, we only display 266 trajectories for 2.5 s (50 frames), from the ~ 7000 trajectories (mean track length 200 frames) acquired during the five minute (6000 frames) experiment duration. We have successfully removed trajectories belonging to ghost and immobile cells (see Fig. 6h).

6 Tracking performance

To assess the accuracy and reliability of our three-dimensional tracking setup and algorithm, we evaluate the system's performance as the number of particles increases. Specifically, we compute the reprojection errors and the lengths of trajectories measured at various suspension concentrations of *C. reinhardtii* cells. Figure 7 illustrates the variation in the number of particles in the images across different concentrations. We found that our object detection algorithm accurately detected particles up to a concentration of 2×10^5 cell/ml (see Fig. 7). At greater concentrations however, some particles were not detected due to overlapping particle images, a common challenge in high density experiments (Schanz et al 2016).

We characterize the particle concentration with the particle source density (N_S) (Barnkob and Rossi 2020; Barnkob et al 2021), a widely used metric in PIV experiments (Adrian et al 2011). The particle source density quantifies the density of particles in each image taking into account the area of the particle image and is calculated as $N_S = N_{\hat{x}}\overline{A_p}/A_I$, where $N_{\hat{x}}$ is the number of particles detected, $\overline{A_p}$ is the average area of the particle images, and A_I is the total area of the image. We used the average measured particle diameter of 9 pixels to determine $\overline{A_p}$, a size that is considerably larger than the typical tracer particle diameter of 2-3 pixels used in typical PIV/PTV measurements (Adrian et al 2011; Schanz et al 2016). The correspondence between the particle concentrations used in our experiments, the average number of detectedparticles, and the source densities are summarized in Table 1. Another commonly used metric, particle image density (particles per pixel, or ppp), provides an alternative way to quantify tracking performance and can be obtained as $N_I = N_S/A_p$.

To calculate the reprojection error, ε_r, we reprojected the triangulated three dimensional particle positions onto

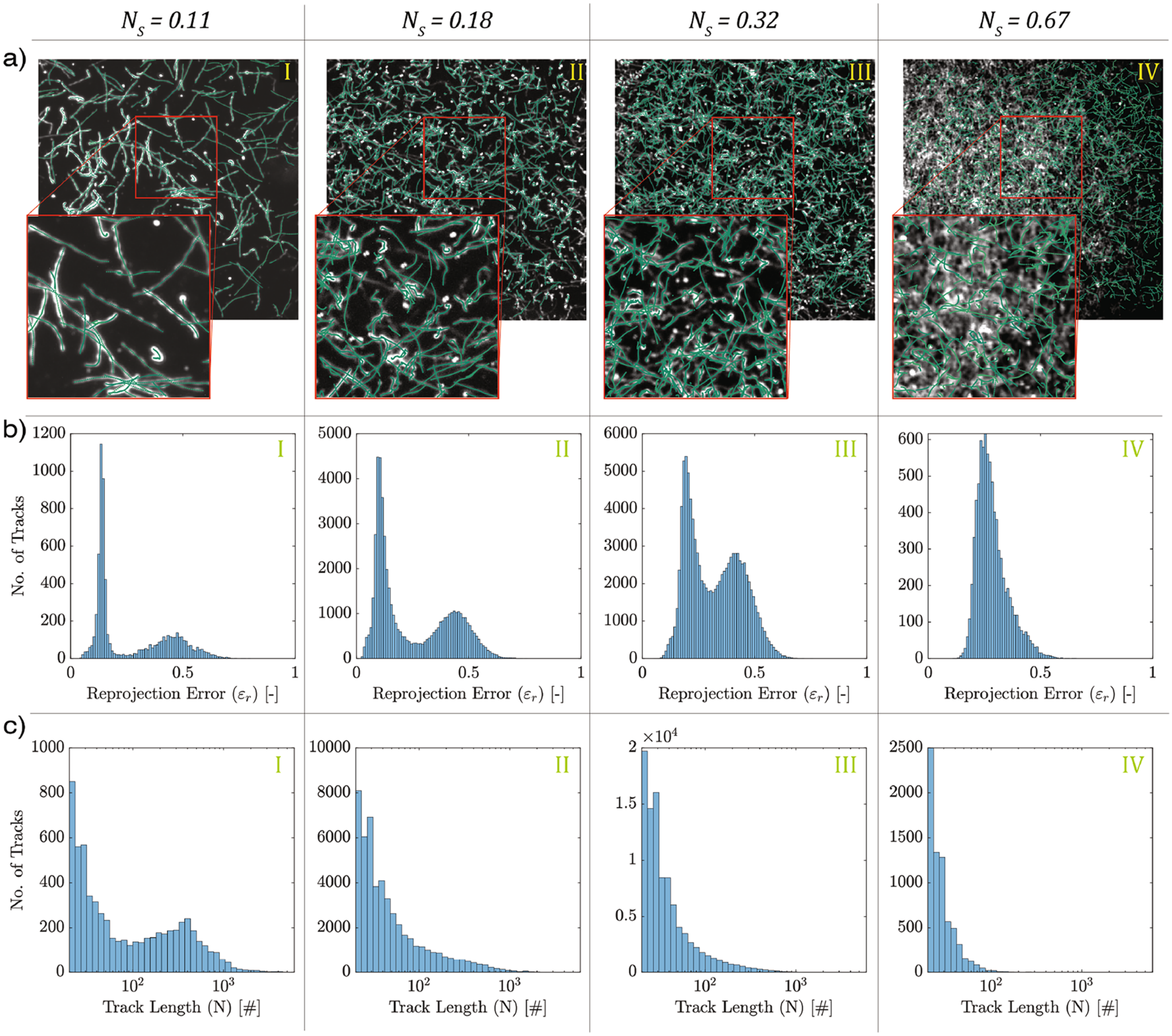

Fig. 8 Tracking performance for varying cell concentrations: I. 5×10^4 cell/ml ($N_S \approx 0.11$), II. 1×10^5 cells/ml ($N_S \approx 0.18$), III. 2×10^5 cells/ml ($N_S \approx 0.32$), IV. 5×10^5 cells/ml ($N_S \approx 0.67$). **a** Composite camera image for 50 frames, overlaid with the re-projected three-dimensional position. Insets show the close-up views of a subsection of each image composite, for clarity. **b** Distributions of time-averaged reprojection error for different cell concentrations. **c** Distributions of track length in terms of number of frames, for each cell concentration

each of the camera images (see Fig. 8a). In principle, the reprojected position should match the center of the detected particle image but in practice these differ due to the skewness of the camera rays. We normalize the distance from the detected particle center to the reprojected location by the size of the particle image. Thus, ϵ_r indicates the deviation of the triangulated position from the imaged center, with a higher value corresponding to more uncertainty. During the time-resolved tracking and optimization step (Sect. 5), a new particle detection is appended to an existing trajectory only if $\epsilon_r < 1$. If this threshold is not met, that detection is not appended, and the trajectory is not extended further. Consequently, ϵ_r in our final dataset ranges from 0 to 1.

We report the distribution of time-averaged trajectory reprojection errors in Fig. 8b for various image densities. The reprojection error exhibits a bimodal distribution for all image densities except the highest tested at $N_S = 0.67$, with the first peak around $\epsilon_r \approx 0.15$ representing correctly reconstructed particles and the second peak, at $\epsilon_r \approx 0.5$, corresponding to particles with overlapping images or trifocal correspondences instead of quadri-focal. As the N_S increases, the fraction of particles with larger reprojection errors also increases, indicating that the increased occurrence of particle image overlap at higher particle concentrations leads to less reliable reconstruction. The average reprojection error increased from 0.15 to 0.3, with an increase in N_S from 0.11 to 0.32. A reprojection error of 0.3 (equivalent to 0.3 cell diameters, which translates in the context of our *C. reinhardtii* tracking experiments to a positional uncertainty of up to ≈ 3 μm) compares favorably with particle location uncertainties of 1 to 2 cell diameters yielded by holographic tracking techniques imaging particles ranging from 40 to 270 μm in size (Gao et al 2013). At $N_S = 0.67$, particles quickly lose correspondence leading to typically shorter trajectories, many of which are removed during post-processing.

We analyzed the variation in track length as a function of particle source density (see Fig. 8c). At the lowest density $N_S = 0.11$, the average track length was around 200 frames or 10 s. The average track length decreased with increased particle source density. At $N_S = 0.67$, for example, the average track length, N, was only 2 s. This reduction in track length is mainly due to higher occlusion rates at higher image densities, which create ambiguities in unique correspondences and particle detection. As a result, the number of tracked particles was lower than in lower-density data sets, as shown in Fig. 8a-IV, and these particles quickly loose correspondence. Nonetheless, we obtained trajectories at least 5 s long for image densities up to $N_S = 0.32$, sufficient for performing kinematics and population behavior analysis.

Our performance assessment demonstrates that we can reliably track active swimmers up to a particle source density of 0.32, corresponding to 2×10^5 particles/ml. Notably, this is an order of magnitude higher than the concentrations ($1.3-1.7 \times10^4$ particles/ml) that can be accurately tracked using in-line holographic methods for 40 μm particles (Kim and Lee 2008). Recent advances in de-focused particle tracking have enabled the tracking of particles at effective source densities of 0.20–0.24 for 2μm particle sizes, depending on the signal-to-noise ratio (Barnkob and Rossi 2020; Barnkob et al 2021). However, particle image size in defocused setups varies with depth; hence, the particle source density does not remain constant throughout the recording sequence. In contrast, the size of the particle image is constant in our approach and the particle image density (N_I) offers a more direct method of comparison. Although the defocused particle tracking method achieves an effective N_I of about 0.0011ppp (Barnkob and Rossi 2020; Barnkob et al 2021), our system reaches approximately 0.005ppp at a particle source density of 0.32, which is substantially greater.

Modern macroscopic 3D tracking systems with multiple cameras and the shake-the-box (STB) algorithm (Schanz et al 2016; Huhn et al 2017; Jahn et al 2021) can reliably track much higher particle source densities up to 0.56, albeit with smaller particle image diameters, around 2-3 pixels. By adapting similar multi-camera principles to a microscopic regime, our setup extends the upper limit of trackable densities in microscale experiments involving bio-active particles, offering a versatile platform for studying a wide range of motile microorganisms under realistic conditions. Moreover, our tracking algorithm results in high throughput of long trajectories with low reprojection error, which provides the basis of our analysis of cell kinematics in this work.

7 Application of multi-camera microscope to cell tracking

The methodology described in Section 2 is ideally suited to investigate the three-dimensional motility of *C. reinhardtii*. In our study, we obtained ~ 45000 trajectories at a concentration of 5×10^4 cells/ml, providing a substantial dataset for analyzing the trajectory kinematics of *C. reinhardtii*.

7.1 Three-dimensional tracking of *C. reinhardtii*

Figure 9 shows examples of three-dimensional trajectories of freely swimming microalgae. Cells display helical motion, which can vary significantly from one cell to another. The majority of the cells move along elongated helices, with

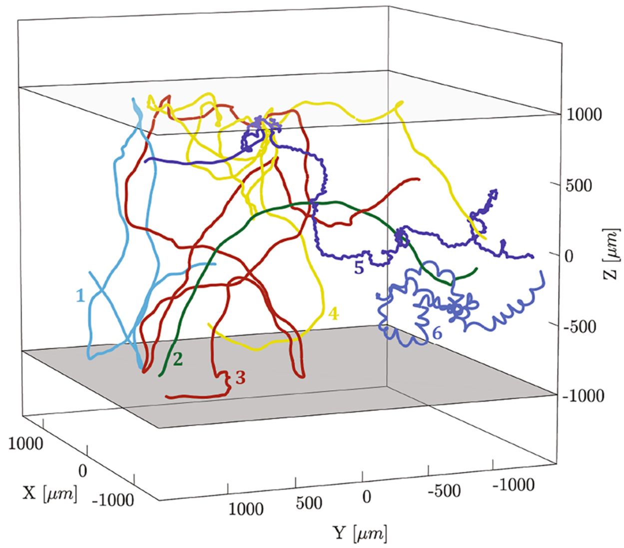

Fig. 9 Six example three-dimensional trajectories of *C. reinhardtii* cells. Light and dark gray shaded regions represent the glass surfaces enclosing the flow chamber

large pitch compared to the helix radius, for example see trajectories 1 to 4. In addition, we observed a few trajectories similar to 5 and 6, characterized by tight helices with short radii and pitch. Our trajectory dataset also highlights a distinct "hopping" behavior near surfaces, represented by trajectory 3, where cells undergo a series of bouncing motions against the surface before moving away. This hopping behavior emerges as a prevalent feature for surface interactions of the microalgae, which we previously examined in detail using the same microscopy setup (Buchner et al 2021).

7.2 Characterization of helical parameters of *C. reinhardtii* trajectories

We first characterized the helical parameters of these trajectories, specifically, velocity V, pitch P, and radius R. To calculate these parameters across all trajectories, we first used piecewise Legendre polynomials to perform a least-squares fit on the discrete trajectory data, $\mathbf{X}_t$, yielding a continuous, time-parameterized curve, $\mathbf{X}(t) = \left[X(t)\ \ Y(t)\ \ Z(t)\right]$, for each trajectory. Next, we used the Frenet–Serret framework to compute the curvature, $\kappa(t)$, and torsion, $\tau(t)$, of

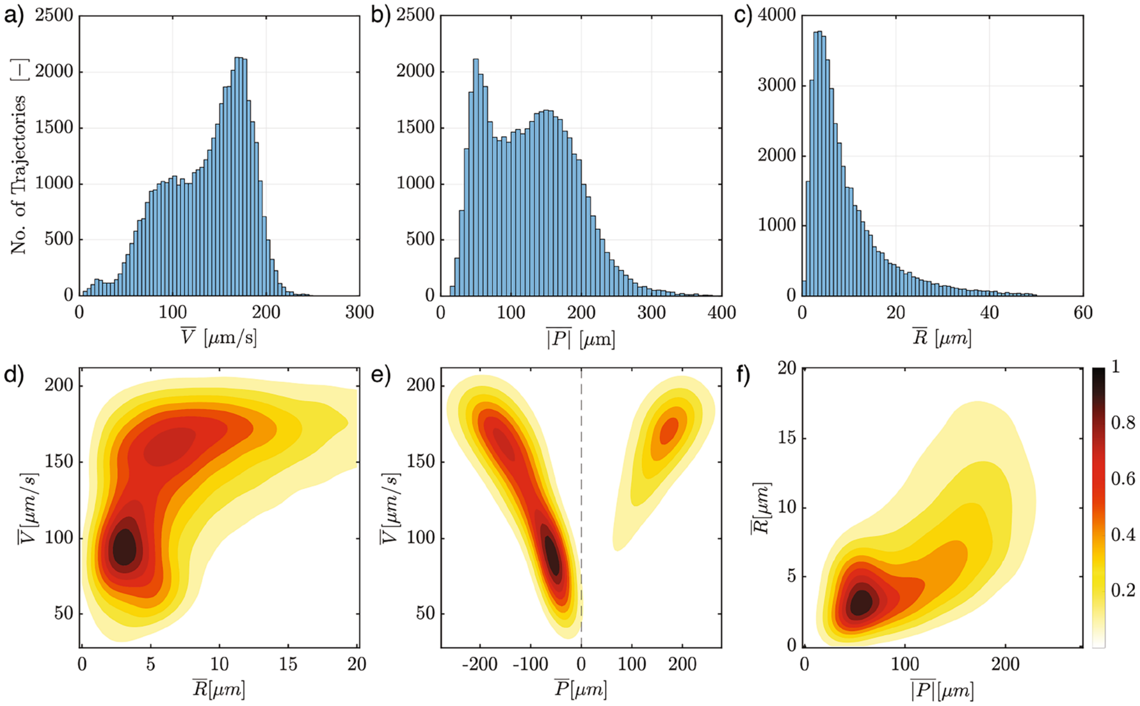

Fig. 10 Top Row: The distributions of time-averaged helical parameters across all trajectories. **a** Velocity, $\overline{V}$ **b** pitch, $\overline{|P|}$, and **c** radius, $\overline{R}$. Bottom Row: 2D joint probability density plots for time-averaged helix parameters for *C. reinhardtii* trajectories. **d** Velocity vs. Radius **e** Velocity vs. Pitch **f** Pitch vs. Radius. The color bar represents the relative density

$\mathbf{X}(t)$ (Crenshaw et al 2000; O'neill 2006). These quantities were then used to compute the helical parameters as:

$$V(t) = \|\mathbf{X}'(t)\|,\; P(t) = \frac{2\pi\tau(t)}{\kappa(t)^2 + \tau(t)^2},\quad \text{and } R(t) = \frac{\kappa(t)}{\kappa(t)^2 + \tau(t)^2}$$

Further details on the piecewise Legendre polynomial fitting and the Frenet–Serret framework can be found in online resource S1.

We then computed time-averaged values for each of the parameters, resulting in one value for each trajectory. Figure 10a presents the distribution of time-averaged velocities, $\overline{V}$, for all trajectories. The distribution is characterized as tri-modal, with peaks centered approximately at 20 μm/s, 90 μm/s, and 160 μm/s. The first mode corresponds to non-motile algae cells drifting in a slow background flow. Excluding the non-motile cells, the remaining predominantly bimodal distribution characterizes the behavior of the healthy motile cells. For our subsequent analysis and discussion, we focus on these cells, specifically those with $\overline{V} \geq 30$ μm/s. The average swimming velocity of *C. reinhardtii* in our experiments was 137 ± 42 μm/s, higher than the average velocities reported by Barry et al (2015), yet similar to the velocity range of $80 - 160\mu$m/s reported by Jin et al (2020). The lower average velocities of 58 ± 24 μm/s from Barry et al (2015) can be attributed to differences in growth conditions, as *C. reinhardtii*'s motility behavior varies depending on these conditions (Harris 2009).

Figure 10b and c presents the distribution of time-averaged absolute pitch, $\overline{|P|}$, and radius, $\overline{R}$, for all trajectories, respectively. The absolute value of the pitch, $|P|$, is used as we are interested in the pitch's magnitude only. The average absolute pitch across all trajectories was $137 \pm 64\mu$m, and the average radius was measured as $8 \pm 7\mu$m, confirming that *C. reinhardtii* cells predominantly follow straighter trajectories, as denoted by the high ratio of average pitch to average radius. The large standard deviations of the measured pitch and radius distributions indicate considerable variability in the motility patterns across the cell population.

We also consider 2D joint distributions of the helical parameters $\overline{V}$, $\overline{P}$, and $\overline{R}$. Figure 10d-f presents these distributions. The joint density plot for velocity and radius (Fig. 10d) demonstrates bimodality across the measured population of individual trajectory-averaged kinematic behavior, with peaks at approximately $\left(\overline{R}, \overline{V}\right) = (4, 90)$ and (6, 160). This suggests the existence of two co-existing populations of cells typified by different swimming characteristics. The faster population exhibits considerably more variation in helical trajectory radius. Over the entire population, it appears that there is a weak nonlinear relationship between $\overline{R}$ and $\overline{V}$, which we quantify via the Spearman's rank correlation coefficient as $r_s = 0.55$. Conversely, the joint distribution of velocity and pitch (Fig. 10e) shows a strong, close to linear, relationship between the two parameters with $r_s = 0.85$. Additionally, we observe that approximately 70% of the algae swim with left-handed chirality ($\overline{P} < 0$), consistent with previous studies (Crenshaw et al 2000).

An important feature of *C. reinhardtii* swimming is the rotation of the cell body around its axis, previously measured at a rate of $1.4 - 2$ Hz (Rüffer and Nultsch 1985). This rotation is due to the beating asymmetry between the cis and trans flagella which, together with the three-dimensional flagellar beating pattern, leads to the characteristic helical motion (Rüffer and Nultsch 1985; Cortese and Wan 2021). Notably, one cell rotation corresponds to one helical turn (Rüffer and Nultsch 1985). Thus, we calculate helical angular velocity to consider variations in cell rotation speeds. Our trajectory data facilitate the computation of this helical angular velocity based on trajectory parameters using the equation:

$$\Omega(t) = \frac{V(t)}{\sqrt{P(t)^2 + R(t)^2}}.$$

The distribution of time-averaged helical angular velocity, $\overline{\Omega}$, for all trajectories in our study is given in Fig. 11, showing that $\overline{\Omega}$ ranges from 0.5 to 2.5 Hz, with an average of 1.23 Hz and standard deviation of 0.36 Hz. As rotation speed directly influences the helical trajectory, a lower rotation speed would result in straighter trajectories, as observed in our experimental data. Furthermore, the spread of angular

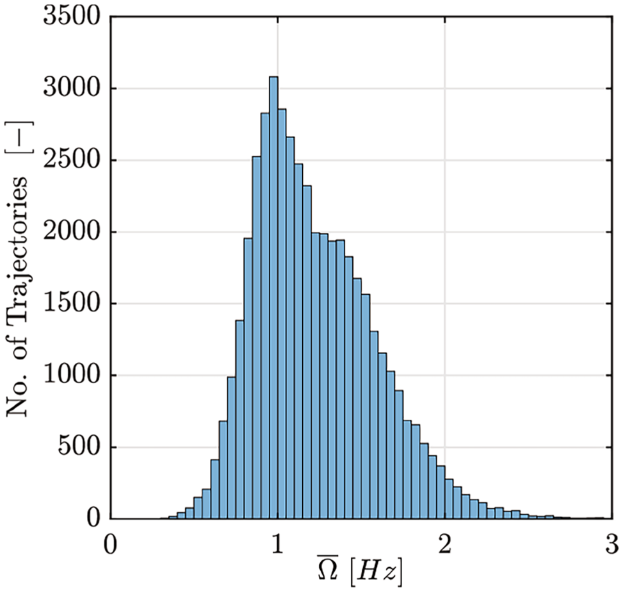

Fig. 11 The distribution of time-averaged angular velocity, $\overline{\Omega}$, for all of the trajectories

velocities indicates that not all cells rotate at the same speed but experience different rotation velocities. This could be due to the differences in force asymmetries that each algal cell experiences. Angular velocity in our experiments is slightly lower than the previously measured rotation speed from Rüffer and Nultsch (1985). The *C. reinhardtii* strain used in their study differed from ours, which could explain the difference in the values.

The motility of *C. reinhardtii* cells has been shown to exhibit a certain level of stochasticity, which varies with environmental conditions (Polin et al 2009; Kurtuldu et al 2013). The asynchronous flagellar beating pattern causes stochastic sharp turns during the cell's motion and is responsible for a run-and-tumble random walk (Polin et al 2009), which leads to a diffusive behavior on longer time scales. We computed the reorientation time τ_P and persistence length L_P of the cell's motion using our extensive trajectory data set to characterize this behavior. The reorientation time τ_P characterizes the time scale at which the cell changes direction, and the persistence length L_P, which is directly deduced from τ_P, characterizes the length scale over which the cell's swimming direction remains correlated. In polymer physics, the persistence length is commonly used to measure the chain's rigidity or flexibility, quantifying the distance over which the orientation of the bonds persists (Zhang et al 2019). Here, we use L_P as a measure of how far the cell moves before it deviates from a straight path and loses memory of its initial swimming direction. We thereby characterize how the swimming direction evolves with distance traveled, ultimately diverging from the initial direction beyond this characteristic length scale. Additionally, we calculated the translational and rotational diffusion coefficients to further describe the diffusive behavior of the cell motion.

To calculate the reorientation time, τ_P, we derive an expression for the mean squared displacement (MSD) of a cell, assuming the correlation function of the swimming direction decays exponentially with a characteristic timescale, τ_P. This timescale marks the crossover from ballistic to diffusive regimes. In the ballistic regime, applicable at short timescales where $t \ll \tau_P$, the MSD scales as Δt^2. Conversely, at longer timescales where $t \gg \tau_P$, the motion is diffusive, and the MSD scales linearly with Δt.

The MSD is expressed by the equation:

$$\mathrm{MSD}(\Delta t) = 2\langle V^2\rangle \Delta t \tau_p \left[1 - \frac{\tau_p}{\Delta t}\left(1 - e^{-\frac{\Delta t}{\tau_P}}\right)\right]. \tag{7}$$

Here, $\langle V^2\rangle$ is the mean squared velocity of the cell. A detailed description of our model is provided in online resource S1. We compute the MSD for all trajectories in our experiments as $\mathrm{MSD}(\Delta t) = \langle |\mathbf{X}(\Delta t + t_\circ) - \mathbf{X}(t_\circ)| \rangle$, and τ_p is determined by fitting Eq. 7 to our data as illustrated in Fig. 12. Following this, we computed the persistence length and translational and rotational diffusion coefficients as:

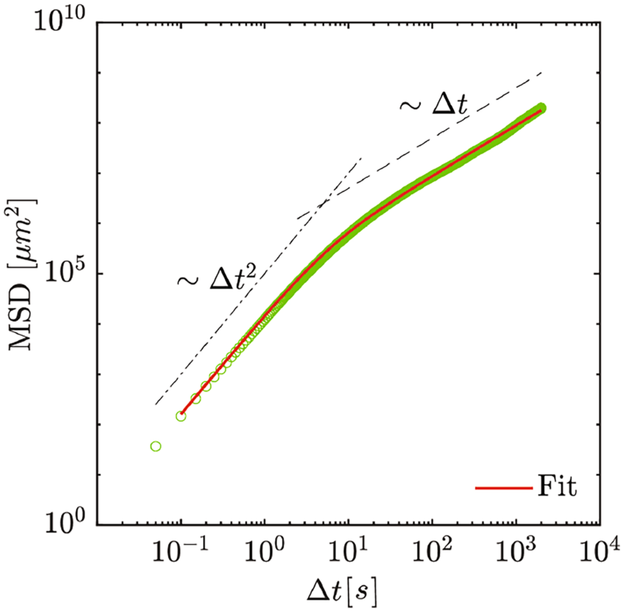

Fig. 12 Mean square displacement (MSD) for *C. reinhardtii* three-dimensional trajectories as a function of Δt. The solid red line shows the fit of Eq. 7 used to determine reorientation time (τ_P)

$$L_P = \sqrt{\langle V^2\rangle}\tau_P, \quad D_T = \frac{L_P^2}{3\tau_P}, \text{ and } \quad D_R = \frac{1}{2\tau_P}.$$

Table 2 presents the diffusion parameters investigated in this study. Our findings regarding these parameters are consistent with previous research, indicating the reliability of our measurements. The observed average persistence length of approximately 729 μm suggests that *C. reinhardtii* cells move along relatively straight paths. Furthermore, our study emphasizes the importance of considering dimensions when making measurements, as evidenced by the contrasting translational diffusion coefficients obtained from 2D and 3D studies. Specifically, our measurement yielded a translational diffusion coefficient of $3.77 \times 10^4\ \mu\ \mathrm{m}^2$/s, which is higher than the $5.56 \times 10^3\ \mu\ \mathrm{m}^2$/s reported in a 2D measurement by Barry et al. (2015). However, our translational diffusion coefficient closely aligns with the value reported in a 3D study conducted by Polin et al (2009).

7.3 *C. reinhardtii's* phototactic response

Phototaxis, or the movement of an organism in response to light, is a well-documented behavior in many microorganisms (Foster and Smyth 1980; Foster et al 1984). *C. reinhardtii* is known to display phototaxis under light

Table 2 Diffusive characteristics of *C. reinhardtii* cells swimming in Tris medium at 5×10^4 cells/ml concentration

Parameter	Present work	Previous studies
Re-orientation time (τ_P) [s]	4.7	11.2 (Polin et al 2009), 10.8 (Liu et al 2020)
Persistence length (L_P) [μm]	729	-
Translational diffusion coefficient (D_T) [μm^2/s]	3.77×10^4	4.7×10^4 (Polin et al 2009), 5.56×10^3 (Barry et al 2015)
Rotational diffusion coefficient (D_R) [rad^2/s]	0.106	0.15 (Barry et al 2015; Drescher et al 2011)

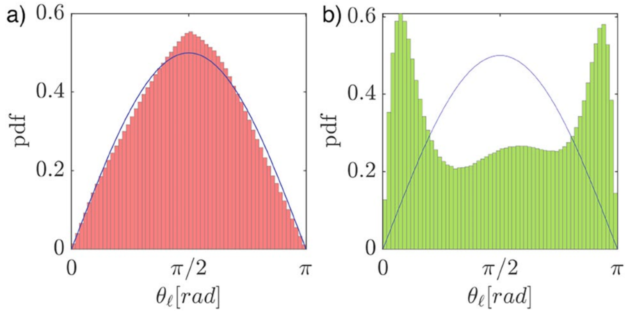

Fig. 13 Comparison of the distributions of algae cell orientation relative to light direction under (**a**) red and (**b**) green wavelengths. The solid blue line represents the theoretical distribution, given by $\sin(\theta_\ell)/2$, for a particle moving randomly in three dimensions

wavelengths ranging from 420-500 nm (Crescitelli et al 1992). Using our experimental setup, we conducted exploratory analyses on the phototactic response of *C. reinhardtii* to two different wavelengths: 650 nm (red) and 500 nm (green) laser light for cell concentration of 5×10^4 cells/ml.

In our experimental design, the light source's positioning ensured the incoming light rays aligned along the negative z-axis (Fig. 1b). We calculated the algae cells' orientation angle θ_ℓ using $\theta_\ell = \cos^{-1}\left(-V_z(t)/\|\mathbf{V}(t)\|\right)$, where $\mathbf{V}(t) = (V_x(t), V_y(t), V_z(t))$ is the instantaneous velocity vector and $-V_z(t)$ is negative of the Z-component of the velocity vector, accounting for the negative Z-axis alignment of the light rays.

Figure 13 presents the distribution of θ_ℓ for all of the algae cells for all the time steps for both red (650 nm) and green (500 nm) light wavelengths. There is a marked contrast in the distribution between red and green cases. Under red illumination, the orientation distribution peaks at $\theta_\ell = \pi/2$, suggesting the cells swim without any specific direction preference. This orientation matches the expected distribution for an isotropic system, as indicated by the solid blue lines. Under green light however, the algae swim predominantly parallel or opposite to the light direction as shown by peaks around $\theta_\ell = 0$ and $\theta_\ell = \pi$. These findings are in agreement with previous research on the phototaxis of *C. reinhardtii*, which demonstrated that *C. reinhardtii* cells show no preferred direction at longer wavelengths, while at shorter wavelengths, they exhibit a preferred direction either toward or away from the light (Schaller et al 1997; Foster et al 1984).

8 Conclusion

This paper presents a three-dimensional tracking setup and algorithm that accurately and reliably tracks the motion of microswimmers, specifically the unicellular green alga *C. reinhardtii*. Our system represents a significant advancement over previous microswimmers tracking methods, achieving reliable tracking even at higher particle source density of 0.32 compared to single-camera microscopy approaches. Our algorithm generates long trajectories with low reprojection error, enabling detailed analysis of trajectory kinematics.

Analysis of our tracking data reveals that *C. reinhardtii* cells exhibit helical swimming patterns with varying radii and pitch, as illustrated in Fig. 9. Most cells swim in elongated helices with larger pitch and shorter radii. Additionally, we find that approximately 70% of the algae swim with left-handed chirality, consistent with previous studies. We also determine the helical angular velocity, with an average value of 1.23 ± 0.36 Hz. Lower rotation speeds result in more linear trajectories, and variations in rotation speeds among cells suggest individual differences in flagellar force asymmetries.

We characterize the diffusive behavior of *C. reinhardtii* cells by calculating parameters such as reorientation time, persistence length, translational diffusion coefficients, and rotational diffusion coefficients. Our investigation of diffusion parameters reaffirms the consistency of our measurements with previous research. Importantly, we highlight the significance of considering dimensions when quantifying diffusion. Specifically, our 3D measurement yields a translational diffusion coefficient one order of magnitude higher than that previously reported in 2D measurements by Barry et al (2015). These findings underscore the necessity of accounting for the three-dimensional nature of cell motion, as relying solely on a 2D approach may limit our understanding of cell diffusion behavior.

Finally, we characterized the phototactic response of *C. reinhardtii* cells using two different light sources at wavelengths of 500 nm and 650 nm. Our results showed that in red light (650 nm), the cells swim with no preferred direction, while in shorter-wavelength green light (500 nm), they displayed both positive and negative phototaxis.

Overall, the results of our study demonstrate the effectiveness and versatility of our tracking setup as a powerful tool for investigating the motile behavior of microorganisms with high accuracy. While our system offers significant advantages, it also comes with certain limitations. The requirement for multiple cameras and a shared high-quality main objective adds complexity and cost, making it less accessible compared to other techniques like DPT or HPT. Future work could focus on simplifying the system without compromising tracking accuracy, for example, by exploring alternative optical configurations or computational approaches that reduce the number of required cameras. Despite these challenges, our system provides a robust platform for studying the influence of environmental factors, such as light, gravity, and nutrient availability, on the motility of various microorganisms. These investigations hold significant implications for microbiology, ecology, and biotechnology.

Supplementary Information The online version contains supplementary material available at https://doi.org/10.1007/s00348-025-04002-3.

Acknowledgements This research was supported by the H2020 European Research Council (Grant agreement No. 716712).

Author Contributions We used the definition of contributions according to CRediT (Contributor Roles Taxonomy). JM contributed to conceptualization, methodology, investigation, data curation, formal analysis, visualization, and writing—original draft. KM contributed to conceptualization, methodology, data curation, software, and writing—review. SK contributed to methodology, resources, and visualization. AJB contributed to conceptualization, methodology, investigation, supervision, and writing—review and editing. DT contributed to conceptualization, methodology, investigation, supervision, writing—review and editing, and funding acquisition.

Declarations

Conflict of interest The authors declare that they have no known competing financial interests or personal relationships that could have appeared to influence the work reported in this paper.

References

Adrian L, Adrian RJ, Westerweel J (2011) Particle image velocimetry. 30, Cambridge university press

Alon U, Surette MG, Barkai N et al (1999) Robustness in bacterial chemotaxis. Nature 397(6715):168–171. https://doi.org/10.1038/16483

Attanasi A, Cavagna A, Del Castello L et al (2015) Greta-a novel global and recursive tracking algorithm in three dimensions. IEEE Trans Pattern Anal Mach Intell 37(12):2451–2463. https://doi.org/10.1109/tpami.2015.2414427

Baba SA, Inomata S, Ooya M et al (1991) Three-dimensional recording and measurement of swimming paths of micro-organisms with two synchronized monochrome cameras. Rev Sci Instrum 62(2):540–541. https://doi.org/10.1063/1.1142103

Barnkob R, Rossi M (2020) General defocusing particle tracking: fundamentals and uncertainty assessment. Exp Fluids 61:1–14. https://doi.org/10.1007/s00348-020-2937-5

Barnkob R, Cierpka C, Chen M et al (2021) Defocus particle tracking: a comparison of methods based on model functions, cross-correlation, and neural networks. Measurement Sci Technol 32(9):094011. https://doi.org/10.1088/1361-6501/abfef6

Barry MT, Rusconi R, Guasto JS et al (2015) Shear-induced orientational dynamics and spatial heterogeneity in suspensions of motile phytoplankton. J Royal Soc Interface 12(112):20150791. https://doi.org/10.1098/rsif.2015.0791

Bechinger C, Di Leonardo R, Löwen H et al (2016) Active particles in complex and crowded environments. Rev Modern Phys 88(4):045006. https://doi.org/10.1103/revmodphys.88.045006

Berg HC (1971) How to track bacteria. Rev Sci Instrum 42(6):868–871. https://doi.org/10.1063/1.1685246

Berg HC (2004) E. coli in Motion. Springer New York, NY

Bianchi S, Saglimbeni F, Di Leonardo R (2017) Holographic imaging reveals the mechanism of wall entrapment in swimming bacteria. Phys Rev X 7(1):011010. https://doi.org/10.1103/physrevx.7.011010

Buchner AJ, Muller K, Mehmood J et al (2021) Hopping trajectories due to long-range interactions determine surface accumulation of microalgae. Procee National Acad Sci 118(20):e2102095118. https://doi.org/10.1073/pnas.2102095118

Cheong FC, Wong CC, Gao Y et al (2015) Rapid, high-throughput tracking of bacterial motility in 3D via phase-contrast holographic video microscopy. Biophys J 108(5):1248–1256. https://doi.org/10.1016/j.bpj.2015.01.018

Cierpka C, Kähler CJ (2012) Particle imaging techniques for volumetric three-component (3D3C) velocity measurements in microfluidics. J Visualization 15(1):1–31. https://doi.org/10.1007/s12650-011-0107-9

Coëtmellec S, Buraga-Lefebvre C, Lebrun D et al (2001) Application of in-line digital holography to multiple plane velocimetry. Measurement Sci Technol 12(9):1392. https://doi.org/10.1088/0957-0233/12/9/303

Constantino MA, Jabbarzadeh M, Fu HC et al (2016) Helical and rod-shaped bacteria swim in helical trajectories with little additional propulsion from helical shape. Sci Adv 2(11):e1601661. https://doi.org/10.1126/sciadv.1601661

Coppola S, Kantsler V (2021) Green algae scatter off sharp viscosity gradients. Sci Rep 11(1):1–7. https://doi.org/10.1038/s41598-020-79887-7

Cortese D, Wan KY (2021) Control of helical navigation by three-dimensional flagellar beating. Phys Rev Lett 126(8):088003. https://doi.org/10.1103/PhysRevLett.126.088003

Crenshaw HC (1996) A new look at locomotion in microorganisms: rotating and translating. Am Zoologist 36(6):608–618. https://doi.org/10.1093/icb/36.6.608

Crenshaw HC, Ciampaglio CN, McHenry M (2000) Analysis of the three-dimensional trajectories of organisms: estimates of velocity, curvature and torsion from positional information. J Exp Bio 203(6):961–982. https://doi.org/10.1242/jeb.203.6.961

Crescitelli F, James T, Erickson J et al (1992) The eyespot of Chlamydomonas reinhardtii: a comparative microspectrophotometric study. Vision Res 32(9):1593–1600. https://doi.org/10.1016/0042-6989(92)90152-9

Drescher K, Leptos KC, Goldstein RE (2009) How to track protists in three dimensions. Rev Sci Instrum 80(1):014301. https://doi.org/10.1063/1.3053242

Drescher K, Dunkel J, Cisneros LH et al (2011) Fluid dynamics and noise in bacterial cell-cell and cell-surface scattering. Procee National Acad Sci 108(27):10940–10945. https://doi.org/10.1073/pnas.1019079108

Eisenbach M (1999) Sperm Chemotaxis. Rev Reprod 4(1):56–66. https://doi.org/10.1530/revreprod/4.1.56

Elgeti J, Winkler RG, Gompper G (2015) Physics of microswimmers—single particle motion and collective behavior: a review. Rep Progress phys 78(5):056601. https://doi.org/10.1088/0034-4885/78/5/056601

Elsinga GE, Scarano F, Wieneke B et al (2006) Tomographic particle image velocimetry. Exp fluids 41(6):933–947. https://doi.org/10.1007/s00348-006-0212-z

Feinleid MEH, Curry GM (1971) The relationship between stimulus intensity and oriented phototactic response (topotaxis) in Chlamydomonas. Phys Plantarum 25(3):346–352. https://doi.org/10.1111/j.1399-3054.1971.tb01453.x

Foster KW, Smyth RD (1980) Light antennas in phototactic algae. Microbiol Rev 44(4):572–630. https://doi.org/10.1128/mmbr.44.4.572-630.1980

Foster KW, Saranak J, Patel N et al (1984) A rhodopsin is the functional photoreceptor for phototaxis in the unicellular eukaryote Chlamydomonas. Nature 311(5988):756–759. https://doi.org/10.1038/311756a0

Gao J, Guildenbecher DR, Reu PL et al (2013) Uncertainty characterization of particle depth measurement using digital in-line holography and the hybrid method. Optics Express 21(22):26432–26449. https://doi.org/10.1364/oe.21.026432

Giuliani N, Rossi M, Noselli G et al (2021) How Euglena gracilis swims: flow field reconstruction and analysis. Phys Rev E 103(2):023102. https://doi.org/10.1103/PhysRevE.103.023102

Harkes G, Dankert J, Feijen J (1992) Bacterial migration along solid surfaces. Appl Environ Microbiol 58(5):1500–1505. https://doi.org/10.1128/aem.58.5.1500-1505.1992

Harris EH (2009) The Chlamydomonas Sourcebook: Introduction to Chlamydomonas and Its Laboratory Use: Volume 1, vol 1. Academic press

Hartley R, Zisserman A (2003) Multiple view geometry in computer vision. Cambridge Univ Press. https://doi.org/10.1017/cbo9780511811685

Hill N, Vincent R (1993) A simple model and strategies for orientation in phototactic microorganisms. J Theoretical Bio 163(2):223–235. https://doi.org/10.1006/jtbi.1993.1118

Huesemann MH, Van Wagenen J, Miller T et al (2013) A screening model to predict microalgae biomass growth in photobioreactors and raceway ponds. Biotechnol Bioeng 110(6):1583–1594. https://doi.org/10.1002/bit.24814

Huhn F, Schanz D, Gesemann S et al (2017) Large-scale volumetric flow measurement in a pure thermal plume by dense tracking of helium-filled soap bubbles. Exp Fluids 58:1–19. https://doi.org/10.1007/s00348-017-2390-2

Jahn T, Schanz D, Schröder A (2021) Advanced iterative particle reconstruction for lagrangian particle tracking. Exp Fluids 62:1–24. https://doi.org/10.1007/s00348-021-03276-7

Jin D, Kotar J, Silvester E et al (2020) Diurnal Variations in the Motility of Populations of Biflagellate Microalgae. Biophys J 119(10):2055–2062. https://doi.org/10.1016/j.bpj.2020.10.006

Kantsler V, Dunkel J, Polin M et al (2013) Ciliary contact interactions dominate surface scattering of swimming eukaryotes. Procee National Acad Sci 110(4):1187–1192. https://doi.org/10.1073/pnas.1210548110

Kim H, Große S, Elsinga GE et al (2011) Full 3D–3C velocity measurement inside a liquid immersion droplet. Exp fluids 51(2):395–405. https://doi.org/10.1007/s00348-011-1053-y

Kim H, Westerweel J, Elsinga GE (2013) Comparison of Tomo-Piv and 3D-ptv for microfluidic flows. Measurement Sci Technol 24(2):024007. https://doi.org/10.1088/0957-0233/24/2/024007

Kim S, Lee SJ (2008) Effect of particle number density in in-line digital holographic particle velocimetry. Exp fluids 44:623–631. https://doi.org/10.1007/s00348-007-0422-z

Kurtuldu H, Tam D, Hosoi A et al (2013) Flagellar waveform dynamics of freely swimming algal cells. Phys Rev E 88(1):013015. https://doi.org/10.1103/physreve.88.013015

Lee SJ, Go T, Byeon H (2016) Three-dimensional swimming motility of microorganism in the near-wall region. Exp Fluids 57(2):1–10. https://doi.org/10.1007/s00348-016-2113-0

Leptos KC, Guasto JS, Gollub JP et al (2009) Dynamics of enhanced tracer diffusion in suspensions of swimming eukaryotic microorganisms. Phys Rev Lett 103(19):198103. https://doi.org/10.1103/physrevlett.103.198103

Liu B, Gulino M, Morse M et al (2014) Helical motion of the cell body enhances caulobacter crescentus motility. Procee National Acad Sci 111(31):11252–11256. https://doi.org/10.1073/pnas.1407636111

Liu F, Wu Y, Zeng L (2020) Swimming Characteristics of Chlamydomonas reinhardtii. J Coastal Res 104(SI):455–464. https://doi.org/10.2112/JCR-SI104-081.1

Maas H, Gruen A, Papantoniou D (1993) Particle tracking velocimetry in three-dimensional flows. Exp fluids 15(2):133–146. https://doi.org/10.1007/BF00190953

Malik N, Dracos T, Papantoniou D (1993) Particle tracking velocimetry in three-dimensional flows: Part ii: Particle tracking. Exp fluids 15:279–294. https://doi.org/10.1007/BF00223406

Mathijssen AJ, Figueroa-Morales N, Junot G et al (2019) Oscillatory surface rheotaxis of swimming E coli bacteria. Nature Commun 10(1):3434. https://doi.org/10.1038/s41467-019-11360-0

Meer P, Weiss I (1992) Smoothed differentiation filters for images. J Visual Commun Image Represent 3(1):58–72. https://doi.org/10.1016/1047-3203(92)90030-W

Mitchell DR (2000) Chlamydomonas flagella. J Phycol 36(2):261–273. https://doi.org/10.1046/j.1529-8817.2000.99218.x

Muller K (2023) Tracking Schooling Fish in Three Dimensions: Experiments at the Rotterdam Zoo. PhD thesis, Delft University of Technology, Gildeprint, https://doi.org/10.4233/uuid:12905cc1-b9e7-4bff-972d-19bea5cf4fdf

Muller K, Hemelrijk C, Westerweel J et al (2020) Calibration of multiple cameras for large-scale experiments using a freely moving calibration target. Exp Fluids 61(1):1–12. https://doi.org/10.1007/s00348-019-2833-z

Nakai T, Mouri Y, Goto T (2015) Analysis of the velocity correlation in the collective motion of bacteria. J Aero Aqua Bio-mech 4(1):32–36. https://doi.org/10.5226/jabmech.4.32

O'neill B (2006) Elementary differential geometry. Elsevier

Ouellette NT, Xu H, Bodenschatz E (2006) A quantitative study of three-dimensional lagrangian particle tracking algorithms. Exp Fluids 40:301–313. https://doi.org/10.1007/s00348-005-0068-7

Polin M, Tuval I, Drescher K et al (2009) Chlamydomonas swims with two "gears'in a eukaryotic version of run-and-tumble locomotion. Science 325(5939):487–490. https://doi.org/10.1126/science.1172667

Pottier L, Pruvost J, Deremetz J et al (2005) A fully predictive model for one-dimensional light attenuation by Chlamydomonas reinhardtii in a torus photobioreactor. Biotechnology and Bioengineering 91(5):569–582. https://doi.org/10.1002/bit.20475

Quaranta G, Aubin-Tam ME, Tam D (2015) Hydrodynamics versus intracellular coupling in the synchronization of eukaryotic flagella. Phys Rev Letters 115(23):238101. https://doi.org/10.1103/physrevlett.115.238101

Ralston E, Swain G (2009) Bioinspiration—the solution for biofouling control? Bioinspiration & Biomimetics 4(1):015007. https://doi.org/10.1088/1748-3182/4/1/015007

Rothschild, (1963) Non-random distribution of bull spermatozoa in a drop of sperm suspension. Nature 198(488):1221. https://doi.org/10.1038/200381b0

Rüffer U, Nultsch W (1985) High-speed cinematographic analysis of the movement of Chlamydomonas. Cell motility 5(3):251–263. https://doi.org/10.1002/cm.970050307

Schaller K, David R, Uhl R (1997) How Chlamydomonas keeps track of the light once it has reached the right phototactic orientation. Biophys J 73(3):1562–1572. https://doi.org/10.1016/s0006-3495(97)78188-8

Schanz D, Gesemann S, Schröder A (2016) Shake-The-Box: Lagrangian particle tracking at high particle image densities. Exp fluids 57(5):1–27. https://doi.org/10.1007/s00348-016-2157-1

Shchelik IS, Molino JV, Gademann K (2021) Biohybrid microswimmers against bacterial infections. Acta Biomater 136:99–110. https://doi.org/10.1016/j.actbio.2021.09.048

Sheng J, Malkiel E, Katz J (2006) Digital holographic microscope for measuring three-dimensional particle distributions and motions. Appl optics 45(16):3893–3901. https://doi.org/10.1364/ao.45.003893

Sheng J, Malkiel E, Katz J et al (2007) Digital holographic microscopy reveals prey-induced changes in swimming behavior of predatory dinoflagellates. Proc National Acad Sci 104(44):17512–17517. https://doi.org/10.1073/pnas.0704658104

Speidel M, Jonáš A, Florin EL (2003) Three-dimensional tracking of fluorescent nanoparticles with subnanometer precision by use of off-focus imaging. Optics Lett 28(2):69–71. https://doi.org/10.1364/ol.28.000069

Su TW, Xue L, Ozcan A (2012) High-throughput lensfree 3D tracking of human sperms reveals rare statistics of helical trajectories. Procee National Acad Sci 109(40):16018–16022. https://doi.org/10.1073/pnas.1212506109

Taute K, Gude S, Tans S et al (2015) High-throughput 3D tracking of bacteria on a standard phase contrast microscope. Nature Commun 6(1):1–9. https://doi.org/10.1038/ncomms9776

Wu M, Roberts JW, Buckley M (2005) Three-dimensional fluorescent particle tracking at micron-scale using a single camera. Exp Fluids 38(4):461–465. https://doi.org/10.1007/s00348-004-0925-9

Wu M, Roberts JW, Kim S et al (2006) Collective bacterial dynamics revealed using a three-dimensional population-scale defocused particle tracking technique. Appl Environ Microbiol 72(7):4987–4994. https://doi.org/10.1128/aem.00158-06

Yan G, Solovev AA, Huang G, et al (2022) Soft microswimmers: Material capabilities and biomedical applications. Current Opinion in Colloid & Interface Science p 101609. https://doi.org/10.1016/j.cocis.2022.101609

Yoshimura K, Matsuo Y, Kamiya R (2003) Gravitaxis in Chlamydomonas reinhardtii studied with novel mutants. Plant cell Phys 44(10):1112–1118. https://doi.org/10.1093/pcp/pcg134

Zhang JZ, Peng XY, Liu S et al (2019) The persistence length of semiflexible polymers in lattice monte carlo simulations. Polymers 11(2):295. https://doi.org/10.3390/polym11020295